

ACCEPTED MANUSCRIPT • OPEN ACCESS

## Monitoring the process of formation of ZnO from ZnO<sub>2</sub> using in situ combined XRD/XAS technique.

To cite this article before publication: Thomas Daley *et al* 2021 *J. Phys.: Condens. Matter* in press <https://doi.org/10.1088/1361-648X/abfb91>

### Manuscript version: Accepted Manuscript

Accepted Manuscript is “the version of the article accepted for publication including all changes made as a result of the peer review process, and which may also include the addition to the article by IOP Publishing of a header, an article ID, a cover sheet and/or an ‘Accepted Manuscript’ watermark, but excluding any other editing, typesetting or other changes made by IOP Publishing and/or its licensors”

This Accepted Manuscript is © 2021 The Author(s). Published by IOP Publishing Ltd..

As the Version of Record of this article is going to be / has been published on a gold open access basis under a CC BY 3.0 licence, this Accepted Manuscript is available for reuse under a CC BY 3.0 licence immediately.

Everyone is permitted to use all or part of the original content in this article, provided that they adhere to all the terms of the licence <https://creativecommons.org/licenses/by/3.0>

Although reasonable endeavours have been taken to obtain all necessary permissions from third parties to include their copyrighted content within this article, their full citation and copyright line may not be present in this Accepted Manuscript version. Before using any content from this article, please refer to the Version of Record on IOPscience once published for full citation and copyright details, as permissions may be required. All third party content is fully copyright protected and is not published on a gold open access basis under a CC BY licence, unless that is specifically stated in the figure caption in the Version of Record.

View the [article online](#) for updates and enhancements.

1  
2  
3  
4 Monitoring the process of formation of ZnO from ZnO<sub>2</sub> using in situ combined XRD/XAS technique.  
5  
6  
7

8 Thomas Daley<sup>1</sup>, Kwasi Opuni<sup>1</sup>, Edwin Raj<sup>3</sup>, Andrew J. Dent<sup>2</sup>, Giannantonio Cibin<sup>2</sup>, Timothy I.  
9 Hyde<sup>3</sup> and Gopinathan Sankar<sup>1\*</sup>  
10

11 <sup>1</sup>Department of Chemistry, University College London, 20 Gordon Street, London WC1H 0AJ,  
12 UK  
13

14 <sup>2</sup>Diamond Light Source, Harwell Science & Innovation Campus, Oxfordshire OX11 0DE, UK  
15

16 <sup>3</sup>Johnson Matthey Technology Centre, Blount's Court Sonning Common, Reading RG4 9NH,  
17 UK  
18  
19  
20  
21

22 Corresponding author – [g.sankar@ucl.ac.uk](mailto:g.sankar@ucl.ac.uk)  
23  
24  
25  
26  
27  
28  
29

### 30 **Abstract**

31 Use of in situ combined X-ray diffraction and X-ray absorption spectroscopy for the study of  
32 the thermal decomposition of zinc peroxide to zinc oxide is reported here. Comparison of  
33 data extracted from both X-ray diffraction (XRD) and X-ray absorption spectroscopy (XAS)  
34 with thermo gravimetric analysis (TGA) enabled us to follow the nature of the conversion of  
35 ZnO<sub>2</sub> to ZnO. A temperature range between 230 and 350°C appears to show that a very poorly  
36 crystalline ZnO is formed prior to the formation of an ordered ZnO material. Both the  
37 decrease in white line intensity in the Zn K-edge XANES and resulting lower coordination  
38 numbers estimated from analysis of the Zn K-edge data of ZnO heated at 500°C, in comparison  
39 to bulk ZnO, suggest that the ZnO produced by this method has significant defects in the  
40 system.  
41  
42  
43  
44  
45  
46  
47  
48  
49  
50  
51  
52  
53  
54  
55  
56  
57  
58  
59  
60

## Introduction

Zinc oxide is a multi-functional material that has found a plethora of applications, due to its electronic and structural properties. As an n-type semiconductor, similar to other metal oxides the structure, morphology and size of the particles have a large impact on their properties and uses<sup>[1, 2]</sup>. ZnO is becoming the material of choice for a range of applications which includes transparent conducting oxides<sup>[3-5]</sup>, solar cells<sup>[6-8]</sup>, photocatalytic applications, as a sensing material<sup>[9]</sup> and for antimicrobial applications<sup>[1, 10]</sup>. The defects present in zinc oxide have been proposed to be a key factor for its performance<sup>[3, 11, 12]</sup>.

Nano sized ZnO materials have been synthesised in a variety of ways including hydrothermal<sup>[13]</sup>, mechanochemical<sup>[14]</sup>, spray pyrolysis<sup>[15]</sup>, chemical bath techniques etc<sup>[11, 16-19]</sup>. In addition to the above, ZnO can be conveniently prepared using a two-stage approach by first making zinc peroxide ( $\text{ZnO}_2$ ) and subsequently decomposing this in a controlled way to produce zinc oxide, the method of our choice reported in this work. It has been reported that ZnO prepared via decomposition of  $\text{ZnO}_2$  has defects compared to other methods and it is reported that it is possible to control the types of defects in ZnO which may enhance functionality<sup>[12, 20-22]</sup>.  $\text{ZnO}_2$  on its own found prominent use in the rubber industry for promoting cross-linking in carboxylated nitrile rubber and other elastomers and also as an antiseptic additive<sup>[23, 24]</sup>. The most common method of synthesis of  $\text{ZnO}_2$  is by adding a soluble zinc salt to hydrogen peroxide, while it has also been prepared by hydrothermal or organometallic routes [9,10]. Therefore, it is of considerable interest to follow the decomposition pathway of  $\text{ZnO}_2$  producing ZnO at various temperatures. To follow the decomposition process, it is necessary to use techniques that enable the determination of both long and short-range order. This is required as whilst both the starting  $\text{ZnO}_2$  and final ZnO product are crystalline solids, the decomposition process may not have long-range order and needs to be studied via the use of methods that are suited for the determination of short-range order present in the system. To this end, we have used combined X-ray diffraction (XRD) and X-ray absorption spectroscopy (XAS) at the Zn K-edge to monitor the process of converting crystalline  $\text{ZnO}_2$  to ZnO during a thermal decomposition process. XRD provides information regarding long-range order (crystallinity) whilst XAS (an element specific

1  
2  
3 technique that does not depend on long-range order in a system) yields the required short-  
4 range order information around a given metal ion of interest. In addition, it is well-known  
5 that XRD can be used to determine crystallite size and monitor the formation of  
6 amorphous/poorly crystalline phases. Similarly, XANES has been noted to be sensitive to local  
7 coordination environment<sup>[18]</sup> as well as defects present in systems<sup>[25]</sup>. An added advantage  
8 of using the combined XRD/XAS technique is that it is carried out on the same sample under  
9 identical environment and utilises time-resolved methods in monitoring the changes that take  
10 place rapidly during thermal treatment process<sup>[26-34]</sup>. This combined approach, first  
11 established in early 1990's<sup>[26, 27, 29, 30]</sup>, has become a "work horse" in many Synchrotron  
12 Radiation facilities; a good time-resolution in the measurement of both XRD and XAS  
13 facilitates the process of monitoring the structural changes through temperature or any  
14 reaction coordinate change. Here we report the structural changes and growth process of  
15 ZnO during the thermal decomposition of ZnO<sub>2</sub>, in air employing the *in situ*, time-resolved,  
16 combined XRD/XAS technique.

## 30 Experimental

31 Zinc peroxide was prepared via a wet chemical method. In a typical experiment, 2.0g of zinc  
32 acetate dihydrate was dissolved in 25mL water to which 25mL of 30% H<sub>2</sub>O<sub>2</sub> aqueous solution  
33 was added and stirred. The pH of this solution was adjusted to 10 using dilute NH<sub>4</sub>OH and  
34 stirred for 12 hours at room temperature. The resultant precipitate was isolated by  
35 centrifuging, washed several times with water and dried. X-ray diffraction studies conducted  
36 using a laboratory based, Bruker AXS D8 Advance, X-ray diffractometer operated in parallel  
37 beam mode showed phase pure ZnO<sub>2</sub> material was produced using this method (see  
38 Supplementary information (SI) Figure S1).

39 ICP analysis was carried out on as-synthesised ZnO<sub>2</sub>, commercial ZnO<sub>2</sub> and ZnO samples  
40 heated to 300°C. Assay results confirmed the amount of zinc to be 64.4%, 72.0% and 83.2%,  
41 respectively. Calculated Zn values are 67.1% for pure ZnO<sub>2</sub> and 80.4% for pure ZnO. As  
42 commercial ZnO<sub>2</sub> contains ~50% ZnO, the zinc concentration is expected to be between that  
43 of pure ZnO<sub>2</sub> and ZnO. The obtained value for as-synthesised ZnO<sub>2</sub> is lower than expected  
44 suggesting the presence of impurities. TG/DTA curves for ZnO<sub>2</sub> obtained in air ambient at a  
45 heating rate of 2° C/min are given in Figure 2. The initial weight drop of 2.8% in the  
46 temperature range of 35 – 150°C is possibly due to the loss of adsorbed moisture. A further  
47  
48  
49  
50  
51  
52  
53  
54  
55  
56  
57  
58  
59  
60

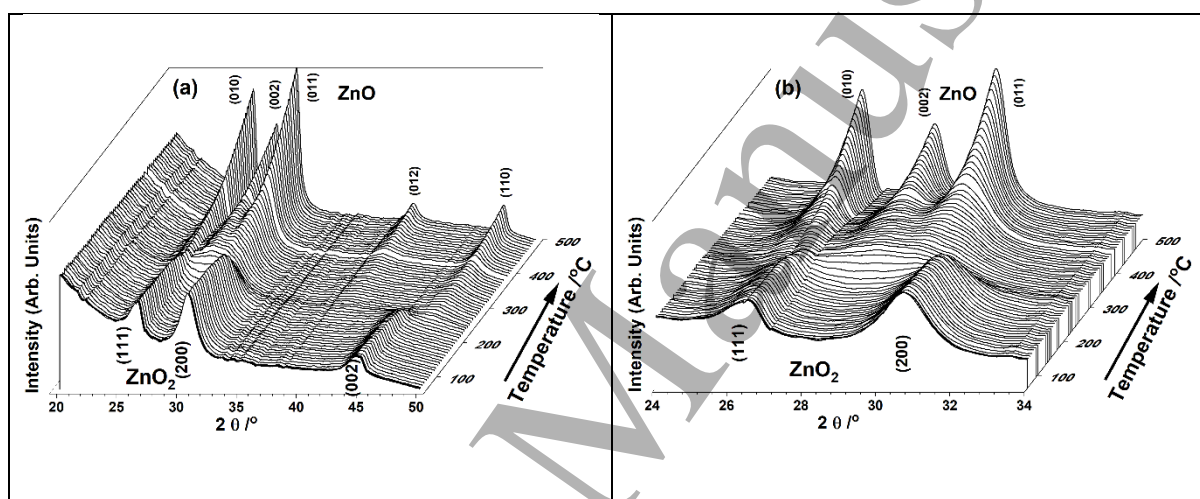
1  
2  
3 15% weight drop in the region of 150 – 250°C corresponds to the decomposition of ZnO<sub>2</sub> to  
4 ZnO (calculated 16.4%).  
5  
6

7  
8 Combined XRD/XAS data were collected on the Zinc K-edge at the B18 beamline, Diamond  
9 Light Source (UK), using a Si (111) monochromator. XAS data was collected at the Zinc K-  
10 edge (energy range 9500 and 10550 eV) using transmission mode, over a period of 35 seconds  
11 using QuEXAFS mode. XRD data was collected using a MYTHEN detector (position sensitive  
12 detector with an angular range of 60° in 2 $\theta$ ) and a data collection time of *ca* 1 second was  
13 used in this work. Overall, with the deadtime associated with the monochromator  
14 movement, 43 seconds elapsed for the combined XRD/XAS measurement. XRD data was  
15 recorded using a wavelength of 1.3051Å, just below the Zn K-edge to avoid any fluorescence  
16 effects. In a typical experiment, 20 mg of zinc peroxide sample was mixed with 130 mg of  
17 inert silica powder (for dilution purposes), ground up and pressed to form a 13 mm pellet.  
18 This pellet was loaded into a high temperature custom built in situ cell (see photograph given  
19 in Supplementary Information, Figure S2) for measuring combined XRD and XAS data.  
20 Measurements were conducted during the heat treatment of the sample in a flow of air at  
21 10ml/min, to 500°C at a rate of 10°C/min and after subsequent cooling to *ca* 50°C.  
22  
23  
24  
25  
26  
27  
28  
29  
30  
31  
32

33  
34 XAS data were processed using suite of ATHENA and ARTEMIS software<sup>[35]</sup>. For Linear  
35 Combination Fitting (LCF) analysis, an option available in the ATHENA software was utilised<sup>[35]</sup>.  
36 Both starting material ZnO<sub>2</sub> and final phase, ZnO (characterised by XRD) were used as  
37 standards for LCF analysis, and the fitting was performed over an energy range of -20 to 80  
38 eV with respect to the Zn K-edge absorption edge of 9661 eV. For determining the local  
39 structural parameters from EXAFS data, a k-range of 2.4 to 10.44 Å<sup>-1</sup> was used. Fitting was  
40 performed in R-space (R-range of 0.8 to 4 Å) using ARTEMIS software<sup>[35]</sup>. The crystal  
41 structures of ZnO<sub>2</sub> and ZnO were used as the starting models and all the relevant paths below  
42 4Å were considered for the fitting methods. The amplitude reduction factor, S<sub>0</sub><sup>2</sup> was  
43 determined to be 0.87 by fixing the Coordination number (CN) to that of crystal structure  
44 data. Inter-atomic distance (R) and Debye-Waller factor ( $\sigma^2$ ) were determined by refining  
45 these parameters along with the E<sub>0</sub> value. Subsequently the S<sub>0</sub><sup>2</sup> value was fixed to determine  
46 change in coordination number. The values of first Zn-O and second Zn-Zn shells were  
47 extracted to determine the local structural change during the thermal decomposition process.  
48  
49  
50  
51  
52  
53  
54  
55  
56  
57  
58  
59  
60

## Results and Discussion

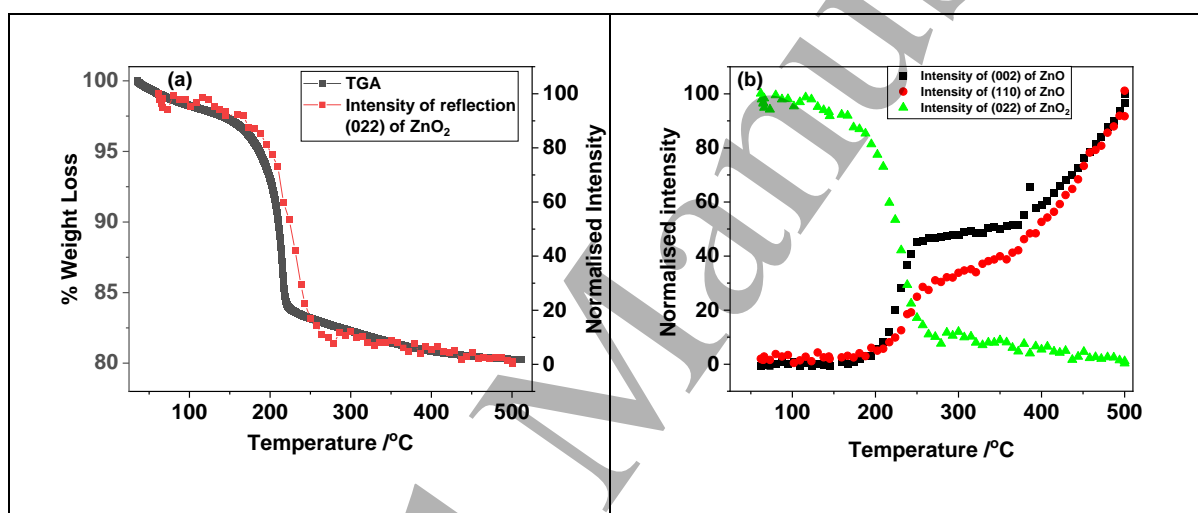
The decomposition of  $\text{ZnO}_2$  was investigated through monitoring the long-range and local structural changes during the heat treatment of  $\text{ZnO}_2$ , employing *in situ* combined XRD/XAS techniques in combination with thermo gravimetric analysis (TGA) methods. In Figure 1 we show a stacked XRD plot recorded through the decomposition of  $\text{ZnO}_2$ . It is seen that the reflections related to  $\text{ZnO}_2$  decrease beyond  $200^\circ\text{C}$  and above  $ca\ 300^\circ\text{C}$  reflections belonging to  $\text{ZnO}$  begin to appear. A TGA plot is shown in Figure 2, wherein it is clear that the weight loss starts to occur gradually just below  $200^\circ\text{C}$ . A sharp decrease of 15% loss is seen above  $200^\circ\text{C}$  and subsequently a slow weight loss takes place before it stabilises.



**Figure 1:** (a) Stacked XRD plot showing the process of decomposition of  $\text{ZnO}_2$  (front) to  $\text{ZnO}$  (back) during thermal treatment on ramping from ambient to  $500^\circ\text{C}$ . (b) the 24 to  $34\ 2\theta$  region of the stacked XRD plot is shown to highlight the nature of  $\text{ZnO}$  formation, in particular highlighting the non-overlapping reflection (independent of any reflection associated with  $\text{ZnO}_2$ ) (002)  $\text{ZnO}$  reflection that occurs at a  $2\theta$  of  $28.99^\circ$ .

To cross correlate these weight losses with changes in the XRD data, we analysed the intense reflections of  $\text{ZnO}_2$  that did not have overlap with  $\text{ZnO}$  reflections to obtain the variation in the intensity of the XRD reflections and plotted these along with the TGA in Figure 2(a) ( $\text{ZnO}_2$  (022) reflection of the XRD data). Although a slight delay in the decrease of the  $\text{ZnO}_2$  reflection intensity is noted here, the exact temperature ramp used for the TGA was different to that used for the combined XAS/XRD experiment. Also, it should also be noted that the XRD measurements were conducted in sequence with respect to the XAS. Furthermore, we anticipate a small temperature difference of  $ca\ 2^\circ\text{C}$  between the point at which the sample

is irradiated with the X-ray beam and the position of the thermocouple placed in the cell (thermocouple is placed *ca* 7 mm away from the beam in order to avoid any interference of the thermocouple with the X-ray beam). However, the trend appears to be closely similar to the weight loss seen in TGA, which we can be attributed to the decomposition of  $\text{ZnO}_2$  and formation of  $\text{ZnO}$  taking place over the temperature range of 175 to 250°C. In Figure 2(b) we compare the intensity variation of the  $\text{ZnO}_2$  (022) reflection and the  $\text{ZnO}$  (002) and (110) reflections, (occurring at the  $2\theta$  values of 28.99 and 47.03 degrees, respectively), that did not overlap with  $\text{ZnO}_2$  reflections. It is apparent that the intensities in this  $2\theta$  range start to appear in the XRD slightly above 200°C whilst the  $\text{ZnO}_2$  reflection intensity begins to decrease around

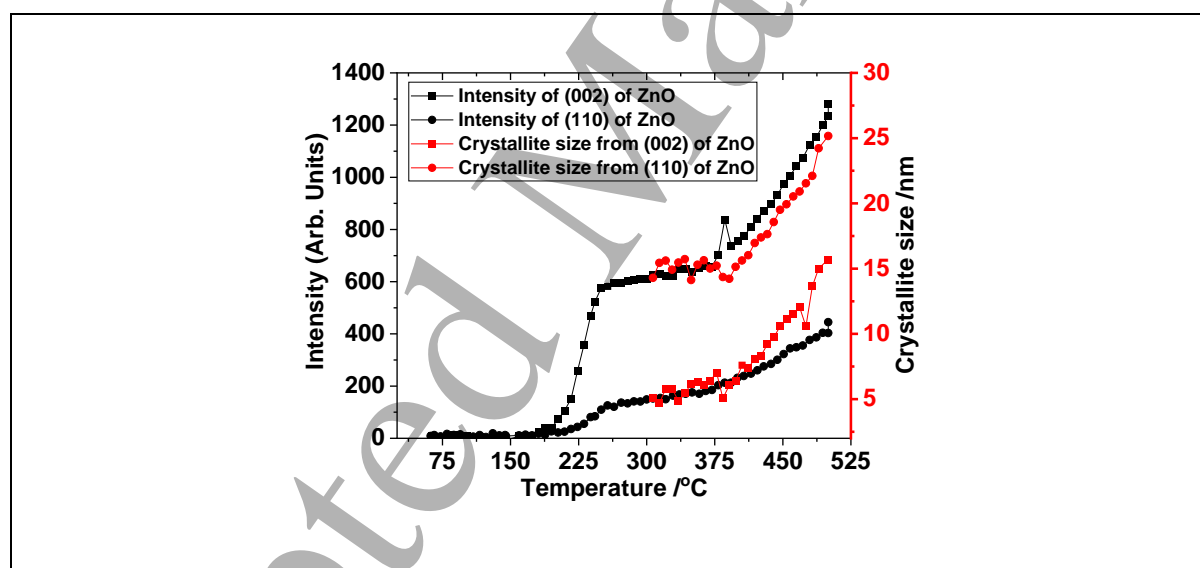


**Figure 2.** (a) TGA curve of  $\text{ZnO}_2$  heated in air and its comparison with the variation in intensity of the  $\text{ZnO}_2$  (022) reflection, determined from Figure 1 (a) with temperature. In Figure 2 (b) we show variation intensity of respective reflections from  $\text{ZnO}_2$  (022) and  $\text{ZnO}$  ( (002) and (110) – corresponding  $2\theta$  positions of 28.99 and 47.03° ) – with temperature. Note that all intensities of these reflections are normalised to 100 of its peak value for ease of comparison and highlight the nature of stagnant growth between *ca* 250 and 350°C.

175°C. Although the  $\text{ZnO}$  reflection intensity at  $2\theta$  of 28.99 and 47.03, seems to increase rapidly at the beginning, closer examination of these specific reflections in the  $2\theta$  range (see Figure 1(b)), suggests that the peaks are very poorly defined and a general increase in the background in this region is seen above 200°C. This implies that very poorly crystalline or

amorphous material is being formed in the initial stages of the decomposition of ZnO<sub>2</sub>. In addition, we noticed that the increase in the intensity values at 2θ of 28.99 and 47.03 for ZnO phase above 250°C remained almost unaltered up to ca 350°C. The intensities of the reflections related ZnO then begin to appear and grow above 350°C,. We interpret this initial increase in intensity values at 2θ of 28.99 and 47.03 around 250°C and subsequent plateau region up to ca 350°C as the result of formation of a poorly crystalline (amorphous like) ZnO material. Above 350°C the ZnO material formed becomes more ordered.

We also determined the crystallite size of the ZnO system by taking the two reflections at 2θ of 28.99 and 47.03, that showed no overlap with ZnO<sub>2</sub> reflections. Full Width at Half Maximum (FWHM) was determined by fitting the peak with a Pseudo Voigt peak function in Origin™ software and these FWHM values were used to determine the crystallite size using the Scherrer equation  $L = \left( \frac{k\lambda}{B\cos(q)} \right)$ . Here, L is crystallite size, B is the full-width at half-maximum



**Figure 3:** Comparison of the normalised intensity of selected ZnO reflections with crystallite size estimated based on the FWHM of selected reflections belonging to ZnO from the X-ray data in Figure 1 (a). Note, only the ZnO reflections that are present above ca 300°C were analysed to estimate the crystallite size.

(FWHM) of a given peak in the XRD pattern at a specific 2θ, λ is the wavelength of incident X-ray and k is a constant. The trend in variation in crystallite size suggests that for temperatures above 350°C, when the ZnO phase shows distinct reflections, the average crystallite size


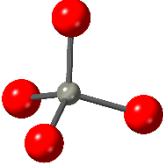


increases to a value close to 30 to 50 nm. The value of crystallite size for the (002) reflection seems higher than the (110) reflection, suggesting a rod type morphology growth taking place in the system which is consistent with hexagonal ZnO.

### Zn K-edge XAS

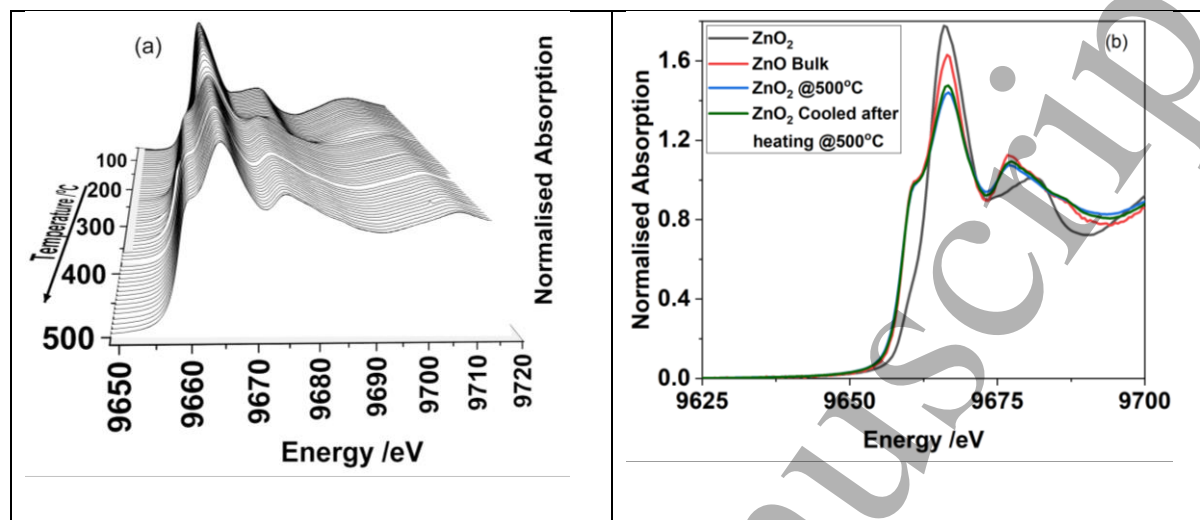
In order to obtain the changes in the short-range order of the system, we analysed the Zn K-edge EXAFS data. To perform XAS data analysis, it is necessary to use related materials as standard and also a starting model for extracting local structural information. Here we used crystalline ZnO<sub>2</sub> and ZnO as our reference ZnO<sub>2</sub> is a crystalline material that crystallises in cubic form (space group *Pa-3*) with cell parameter of  $a = 4.871\text{\AA}$ <sup>[36]</sup>. ZnO crystallises in hexagonal form (*P6<sub>3</sub>mc*) with lattice parameters  $a = 3.2427$   $c = 5.1948\text{\AA}$ <sup>[37]</sup>. The local structure of these systems based on the respective crystal structures are given in Table 1. It

**Table 1:** Local structure of ZnO<sub>2</sub> and ZnO obtained based on the crystal structures given in references 36 and 37. Oxygen in red and Zinc in grey.

System	Crystallographic parameters			Local Structure (first Neighbour)
	Atom-Pair	N	R/ $\text{\AA}$	
ZnO <sub>2</sub> <sup>[36]</sup>	Zn-O	6	2.098	
	Zn-O	6	2.92	
	Zn-Zn	12	3.44	
ZnO <sup>[37]</sup>	Zn-O	4	1.97	
	Zn-Zn	12	3.24	

is clear from Table 1 that ZnO<sub>2</sub> and ZnO have octahedral and tetrahedral environments respectively in the first neighbour coordination. Figure 4 shows a stacked plot of the Zn K-

edge XANES data. Figure 4 (b) shows that the normalised white line intensity (main absorption peak in XANES) is higher for  $\text{ZnO}_2$  compared to  $\text{ZnO}$ , which is related to the local coordination environment.



**Figure 4.** (a) stacked plot of the Zn K-edge XANES recorded during the thermal treatment to 500°C of  $\text{ZnO}_2$ . In (b) we compare the Zn K-edge XANES of  $\text{ZnO}_2$ ,  $\text{ZnO}$  (bulk),  $\text{ZnO}$  (from  $\text{ZnO}_2$ ) at 500°C and the one subsequently cooled to room temperature.

Comparison of the Zn K-edge XANES of  $\text{ZnO}$  obtained from heating  $\text{ZnO}_2$ , clearly shows a reduction in the white line intensity compared to bulk  $\text{ZnO}$  (see Figure 4(b)). It has been reported that the loss in white line intensity can be attributed to vacancies present in the system<sup>[25]</sup>. The overall features in the XANES of  $\text{ZnO}_2$  are different compared to  $\text{ZnO}$  and it is therefore possible to use these two spectra as references to estimate the fractions of  $\text{ZnO}_2$  and  $\text{ZnO}$  phases in the material from the *in situ* data obtained during the thermal treatment process. In Figure 5(a) we show the combination of fractions of spectral features of  $\text{ZnO}_2$  and  $\text{ZnO}$  that matches with the experimental data, recorded during the thermal treatment process. The values obtained, using linear combination fitting analysis of the two reference spectra, plotted against temperature and along with TGA is shown in Figure 5(a). The fraction of  $\text{ZnO}_2$ , estimated from the LCF analysis, at any given stage of the reaction clearly follows the weight loss curve seen in the TGA. The fraction of  $\text{ZnO}$  and  $\text{ZnO}_2$  clearly crosses the mid-point of 50% each in the Figure, which is primarily due to (a) only two reference systems being used and (b) the XAS does not depend on the long-range order. Therefore, irrespective of whether the system is crystalline or amorphous or growing nano crystals, the XANES linear

combination of these two phases appears to represent these states very well at every stage of the thermal process.

Further comparison of the fractions of  $\text{ZnO}_2$  and  $\text{ZnO}$  estimated from LCF analysis of Zn K-edge XANES data were made with the intensities of the XRD reflections representing  $\text{ZnO}_2$  and  $\text{ZnO}$  phases (see Figure 5(b)). Whilst the trend in change in intensity of  $\text{ZnO}_2$  phase in XRD match the fraction estimated from LCF analysis of Zn K-edge XANES data, the intensities of the  $\text{ZnO}$  (002) reflection clearly show differences with the estimated fraction of  $\text{ZnO}$  from XANES.

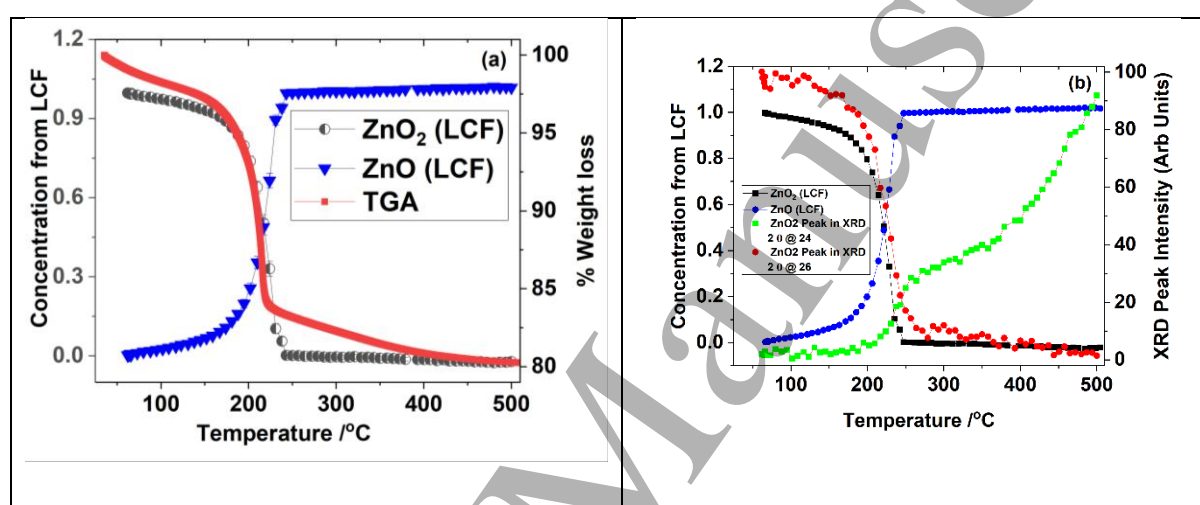


Figure 5: (a) Comparison of fraction of  $\text{ZnO}_2$  and  $\text{ZnO}$  estimated using LCF analysis of Zn K-edge XANES data and the TGA curve (b) Comparison of phase fractions  $\text{ZnO}_2$  and  $\text{ZnO}$  obtained from LCF analysis with intensity variation of  $\text{ZnO}_2$  (022) and  $\text{ZnO}$  (002) reflection from the XRD data (blue).

This demonstrates that as XANES is sensitive to short-range order we start to see changes in the decomposition process at an earlier stage, whereas XRD is unable to follow these changes as it requires the presence of a crystalline phase with a certain degree of long-range order.

We also analysed the EXAFS part of the Zn K-edge XAS data in detail from all the recorded spectrum during the thermal treatment process. A stacked plot of the Fourier Transform (FT) of the Zn K-edge EXAFS data are shown Figure 6(a). There are some clear differences between the data from the beginning of the experiment and above 200°C. In Figure 6(b) we highlight

the changes in the FT after 230°C where it is clear that the second neighbour peak around 3 Å starts to grow.

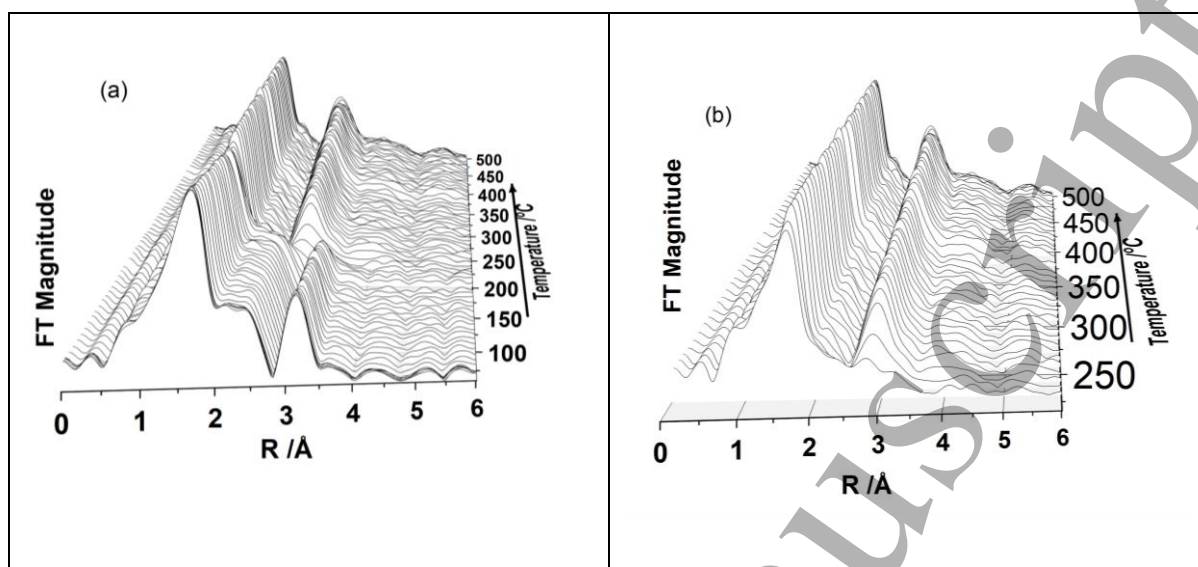
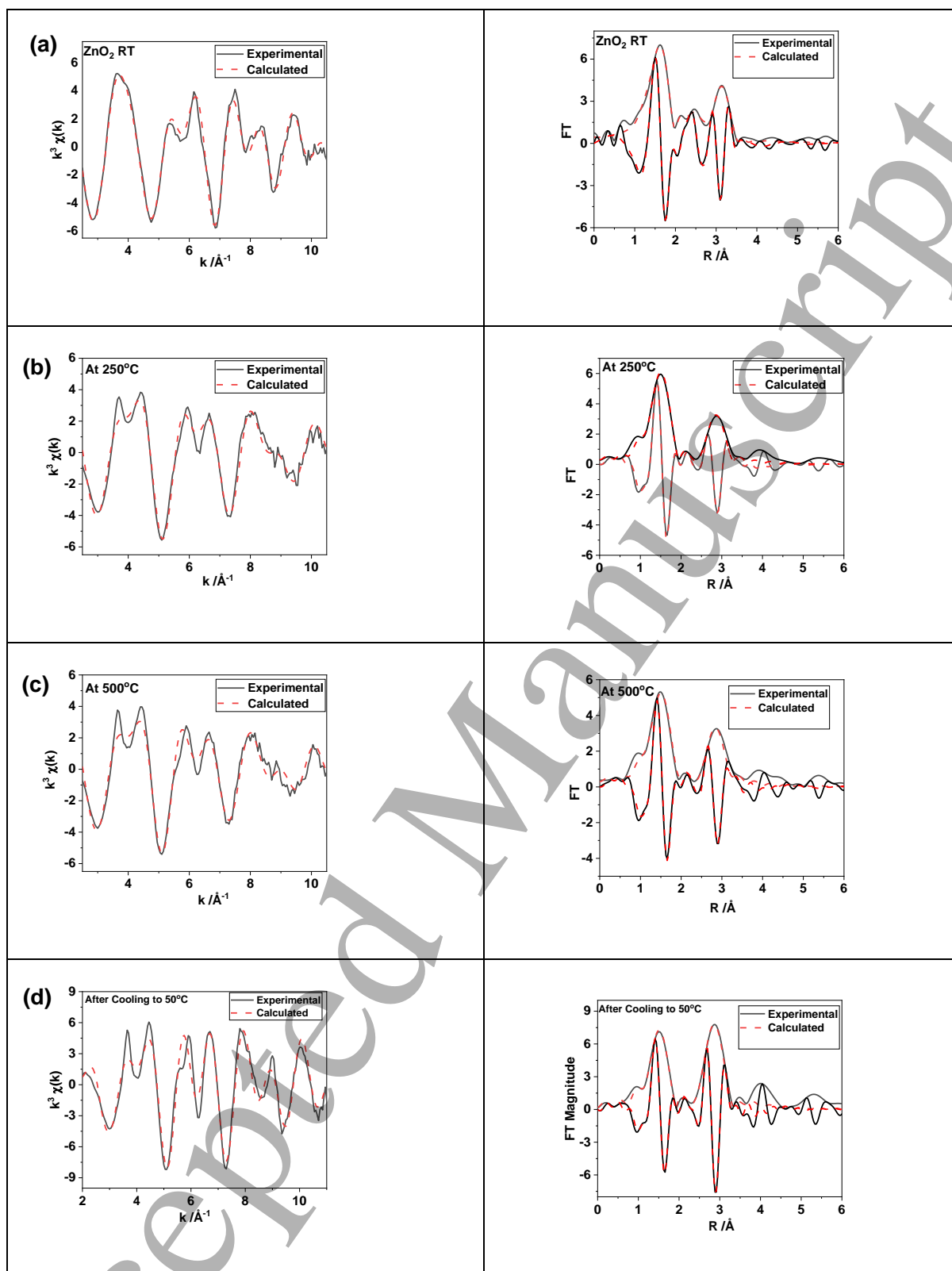


Figure 6: (a) Fourier Transform of the Zn K-edge EXAFS of all data sets recorded during the thermal treatment of ZnO<sub>2</sub> to 500°C (b) only the FT's of the EXAFS data recorded above 250°C are shown for clarity, where only the ZnO phase is present in the system.

We analysed these data sets in detail and representative best fits between experimental and calculated EXAFS after refining parameters in particular, coordination number (CN), interatomic distances and Debye-Waller factors ( $E_0$  was also refined), are given Figure 7. It is clear from the fits that all the short-range order distances are similar to the phases of ZnO<sub>2</sub> and ZnO (given in Table 1) and consistent with the XANES observation for octahedral and tetrahedral coordination environment within the first neighbour distance. In Figure 8(a) we plot the variation in Zn-O and Zn-Zn distances as calculated by EXAFS fitting with the TGA curve. Derived distances clearly follow the decomposition of ZnO<sub>2</sub> resulting in ZnO formation, as the first and second neighbour interatomic distances are distinctly different in these two systems, going from 2.09 Å to ca 1.97 Å for first neighbour Zn-O and 3.44 to 3.22 Å for second neighbour Zn-Zn distance, in agreement with the crystallographic data of ZnO<sub>2</sub> and ZnO, respectively.



**Figure 7:** Selected best fit between experimental and computed EXAFS using parameters listed in Table 1 and associated Fourier Transforms are shown here. (a) RT, (b) 250°C, (c) 500°C and (d) after cooling to 50°C.

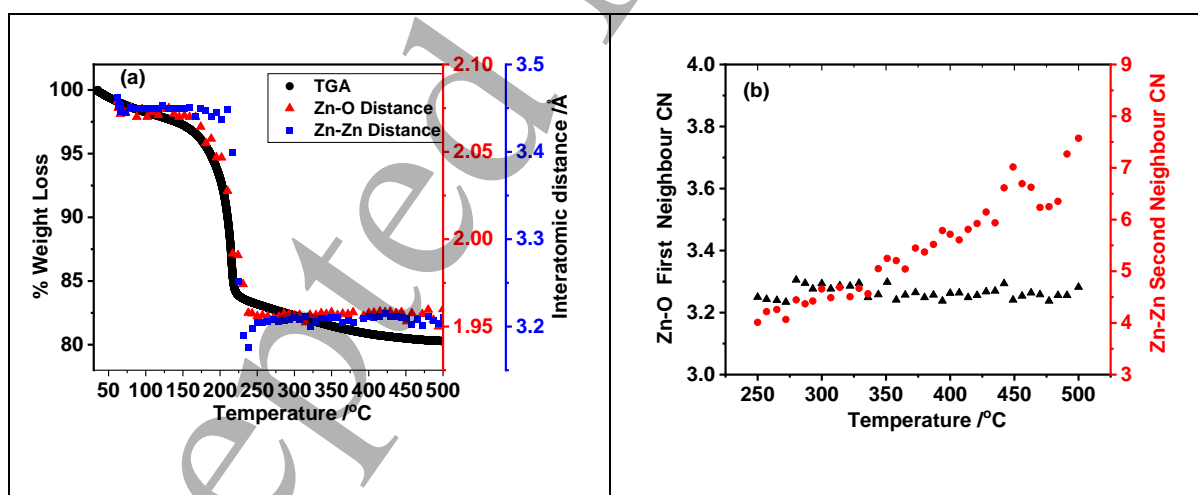
Table 2: Selected structural parameters obtained from best fit between experimental and calculated EXAFS data. N is the average coordination number for the given atom-pair at a distance of R.  $\sigma^2$  is the Debye-Waller factor associated with the atom-pair. The estimated  $S_2$  based on ZnO reference compound is *ca* 0.87

System	Atom-Pair	N	R/Å	$\sigma^2 / \text{Å}^2 \#$	R-Factor
ZnO <sub>2</sub> 30°C	Zn-O	5.9±0.37	2.07±0.02	0.01±0.0013	0.0049
	Zn-O	5.9±0.37	2.94±0.03	0.027±0.004	
	Zn-Zn	12.3±2.8	3.46±0.02	0.016±0.0025	
250°C	Zn-O	3.3 ± 0.19	1.97 ± 0.02	0.006	0.053
	Zn-Zn	4.0 ± 1.1	3.22 ± 0.03	0.017	
500°C	Zn-O	3.3 ± 0.2	1.97 ± 0.02	0.0076	0.046
	Zn-Zn	7.6 ± 1.9	3.22 ± 0.03	0.024	
After Cooling to 50°C	Zn-O	3.3 ± 0.3	1.96±0.02	0.0047±0.0016	0.061
	Zn-Zn	8.6±1.48	3.24±0.03	0.013±0.0015	

# note that analysis of the data recorded at 250 and 500°C were performed by keeping the Debye-Waller factor the same as the ones determined using a reference ZnO material, at these respective temperatures.

Estimating coordination number (essential to understand any defects are present in the system) is difficult as it is highly correlated with the Debye-Waller factor (which has both static and dynamic disorder components). Refining the coordination number (CN) and Debye-Waller factor (DW) together or sequentially of the reference ZnO system as well as the ZnO converted from ZnO<sub>2</sub>, recorded at 500°C, for example, produced both the values well below

what one that is expected for data measured at elevated temperatures. To overcome this issue to estimate whether the coordination number is similar to the bulk or not, we first used a pure crystalline ZnO as our reference to estimate Debye-Waller (DW) factor at any given temperature, by keeping the coordination number (CN) constant at CN of 4 for first Zn-O neighbour and 12 for Zn-Zn second neighbour. We justify as the XRD pattern of the reference ZnO did not change significantly during the heating process (see the stacked XRD, Zn K-edge XANES and FT's of the EXAFS data recorded at different temperatures using identical methods described for ZnO<sub>2</sub> conversion as shown in Supplementary Figures S3, S4 and S5 respectively). This approach indeed assumes that the static disorder contribution in the actual converted samples is similar to bulk ZnO, although the static disorder component may be slightly higher. The estimated DW at various temperatures from the analysis of pure ZnO are shown in the plot for both Zn-O and Zn-Zn neighbours, in the supplementary information (see Supplementary Figure S6); the refined Zn-O and Zn-Zn distances remained closely similar through the analysis at various temperatures. The values of DW at a given temperature were used for the analysis of the Zn K-edge EXAFS data of ZnO (converted from ZnO<sub>2</sub>) from *ca* 250°C and above and extracted the CN values for ZnO at a given temperature. Plot of the variation in CN with temperature is shown in Figure 8(b). It is found that both the CN of Zn-O and Zn-Zn first



**Figure 8(a)** Comparison of TGA curve (grey) with change in Zn-O (red) and Zn-Zn (blue) interatomic distances, as calculated from EXAFS fitting with temperature. In (b) we show the variation in coordination number (CN) with temperature for the first Zn-O and second Zn-Zn neighbours. Note that the error in estimating CN is *ca* 10% or lower for the first Zn-O

1  
2  
3 coordination whereas the error for 2<sup>nd</sup> neighbour appears to be larger, in the range of 20 to  
4  
5 30%.

6  
7  
8 and second neighbours were found to be below the expected values compared to a bulk  
9 highly crystalline solid. Whilst the CN values of Zn-O is around 3.5, the values for the second  
10 neighbour in the high temperature data above 250°C appears to be much smaller compared  
11 to the bulk ZnO and slowly increased to ca 8 for the second neighbour Zn-Zn coordination.  
12 This could be due to defects present in the system which becomes less when heated at  
13 temperatures above 400°C. In order to confirm whether this reduction is due temperature,  
14 the thermally treated sample measured after cooling to ca 50°C was also analysed and the  
15 results are shown in Table 2 and the best fit for this data are shown in Figure 7(d). Indeed,  
16 the coordination number for both Zn-O and Zn-Zn remain at a lower value compared to the  
17 bulk while the DW factor decreased, as one would expect for the sample cooled close to 30°C.  
18 However, nano crystalline oxides also show lack of higher neighbour contributions due to size  
19 effects<sup>[11, 38]</sup> It is difficult to determine or suggest whether such a decrease in CN values of  
20 higher neighbours is related to the presence of defects or nano crystalline form or both, as it  
21 was shown that additional methods are required to differentiate this aspect.<sup>[38]</sup> Combining  
22 the observations that the decrease in the white-line intensity seen in the XANES (Figure 4(b))  
23 and the decreased average CN values of both first and second neighbour coordination  
24 environments suggests that the ZnO formed by thermal decomposition produces a defective  
25 material and possibly in addition to being a nano system consistent with earlier studies.<sup>[13, 25,</sup>  
26  
27  
28  
29  
30  
31  
32  
33  
34  
35  
36  
37  
38  
39  
40  
41 39]

42  
43 In summary, we used a rapid EXAFS and diffraction measurement technique which provided  
44 high quality EXAFS data to determine the thermal decomposition of ZnO<sub>2</sub> material to ZnO.  
45 The combined technique, performed in situ, allowed us to determine the pathway to the  
46 conversion of ZnO material. By comparing the results with the TGA and the techniques  
47 representing long and short-range order of the system, we have been able to identify a region  
48 where amorphous or very poorly crystalline ZnO solid is formed. Comparison of the XANES  
49 and the EXAFS results with the bulk ZnO suggest that defects are present in the system formed  
50 from decomposition of the ZnO<sub>2</sub>, however further work is necessary to provide further  
51 evidence for the nature of the defects present in the system. The results reported in this work  
52 could be used to synthesise a ZnO system, which can be studied for applications as



semiconductors (including as transparent conduction oxide), with various degrees of crystallinity; poorly crystalline<sup>[40]</sup> and defective ZnO.

## Acknowledgement

We thank EPSRC, Johnson Matthey for funding the PhD studentship to TD. We also thank Diamond Light source for providing facilities and beam time (SP6966-1). We thank Dr Diego Gianolio for useful discussions. We would like to dedicate this manuscript to late Professor Neville Greaves who was the driving force in implementing the combined XRD/XAS technique in 1990's, in the UK.

## References

- [1] Theerthagiri J, Salla S, Senthil R A, et al. *Nanotechnology* 2019 **30** 392001
- [2] Borysiewicz M A *Crystals* 2019 **9** 505
- [3] Bhachu D S, Sankar G and Parkin I P *Chemistry of Materials* 2012 **24** 4704-4710
- [4] Dixon S C, Sathasivam S, Williamson B A D, et al. *Journal of Materials Chemistry C* 2017 **5** 7585-7597
- [5] Chen Y Q and Iop "Review of ZnO Transparent Conducting Oxides for solar applications" *4th International Conference on Applied Materials and Manufacturing Technology* 2018.
- [6] Wibowo A, Marsudi M A, Amal M I, et al. *Rsc Advances* 2020 **10** 42838-42859
- [7] Wu W Q, Chen D H, Caruso R A, et al. *Journal of Materials Chemistry A* 2017 **5** 10092-10109
- [8] Yeoh M E and Chan K Y *International Journal of Energy Research* 2017 **41** 2446-2467
- [9] Beitollahi H, Tajik S, Nejad F G, et al. *Journal of Materials Chemistry B* 2020 **8** 5826-5844
- [10] Sehmi S K, Lourenco C, Alkhuder K, et al. *Acs Infectious Diseases* 2020 **6** 939-946
- [11] Liew L L, Sankar G, Handoko A D, et al. *Journal of Solid State Chemistry* 2012 **189** 63-67
- [12] Wang J, Chen R S, Xiang L, et al. *Ceramics International* 2018 **44** 7357-7377
- [13] Rodrigues J, Medeiros S, Vilarinho P M, et al. *Physical Chemistry Chemical Physics* 2020 **22** 8572-8584
- [14] Rumyantsev R N, Mel'nikov A A, Batanov A A, et al. *Glass and Ceramics* 2021 **77** 400-404
- [15] Tani T, Mädler L and Pratsinis S E *Journal of Nanoparticle Research* 2002 **4** 337-343
- [16] Cao B and Cai W *The Journal of Physical Chemistry C* 2008 **112** 680-685
- [17] Handoko A D, Liew L L, Lin M, et al. *Nano Research* 2018 **11** 2412-2423
- [18] McPeak K M, Becker M A, Britton N G, et al. *Chemistry of Materials* 2010 **22** 6162-6170
- [19] McPeak K M, Le T P, Britton N G, et al. *Langmuir* 2011 **27** 3672-3677
- [20] Li X M, Song J Z, Liu Y L, et al. *Current Applied Physics* 2014 **14** 521-527
- [21] Chen W, Lu Y H, Wang M, et al. *Journal of Physical Chemistry C* 2009 **113** 1320-1324
- [22] Rosenthal-Toib L, Zohar K, Alagem M, et al. *Chemical Engineering Journal* 2008 **136** 425-429
- [23] Ibarra L and Alzorriz M *Journal of Applied Polymer Science* 2002 **86** 335-340
- [24] Ibarra L and Alzorriz M *Journal of Applied Polymer Science* 2002 **84** 605-615
- [25] Haug J, Chasse A, Dubiel M, et al. *Journal of Applied Physics* 2011 **110** 063507
- [26] Clausen B S, Grabaek L, Steffensen G, et al. *Catalysis Letters* 1993 **20** 23-36
- [27] Clausen B S, Steffensen G, Fabius B, et al. *Journal of Catalysis* 1991 **132** 524-535

- 1  
2  
3 [28] Clausen B S, Topsoe H and Frahm R "Application of combined X-ray diffraction and  
4 absorption techniques for in situ catalyst characterization" In: D. D. Eley, W. O. Haag, B.  
5 Gates and H. Knozinger, eds. *Advances in Catalysis, Vol 42* 1998:315-344.  
6  
7 [29] Couves J W, Thomas J M, Waller D, et al. *Nature* 1991 **354** 465-468  
8 [30] Dent A J, Wells M P, Farrow R C, et al. *Review of Scientific Instruments* 1992 **63** 903-906  
9 [31] Sankar G, Thomas J M, Rey F, et al. *Journal of the Chemical Society-Chemical*  
10 *Communications* 1995 2549-2550  
11 [32] Sankar G, Wright P A, Natarajan S, et al. *Journal of Physical Chemistry* 1993 **97** 9550-9554  
12 [33] Thomas J M and Greaves G N *Catalysis Letters* 1993 **20** 337-343  
13 [34] Sankar G, Dent A J, Dobson B, et al. *Journal of Non-Crystalline Solids* 2016 **451** 16-22  
14 [35] Ravel B and Newville M *Journal of Synchrotron Radiation* 2005 **12** 537-541  
15 [36] Puselj M, Ban Z and Morvaj J *Croatica Chemica Acta* 1985 **58** 283-288  
16 [37] Schulz H and Thiemann K H *Solid State Communications* 1979 **32** 783-785  
17 [38] Marchbank H R, Clark A H, Hyde T I, et al. *Chemphyschem* 2016 **17** 3494-3503  
18 [39] Kuzmin A and Chaboy J *Iucrj* 2014 **1** 571-589  
19 [40] Zubkins M, Gabrusenoks J, Chikvaidze G, et al. *Journal of Applied Physics* 2020 **128** 8  
20  
21  
22  
23  
24  
25  
26  
27  
28  
29  
30  
31  
32  
33  
34  
35  
36  
37  
38  
39  
40  
41  
42  
43  
44  
45  
46  
47  
48  
49  
50  
51  
52  
53  
54  
55  
56  
57  
58  
59  
60